THE JOURNAL OF PHYSICAL CHEMISTRY LETTERS
A JOURNAL OF THE AMERICAN CHEMICAL SOCIETY

pubs.acs.org/JPCL

Letter

Physical Vapor Deposition Features of Ultrathin Nanocrystals of $Bi_2(Te_xSe_{1-x})_3$

Dmitry S. Yakovlev, Dmitry S. Lvov, Olga V. Emelyanova, Pave S. Dzhumaev, Igor V. Shchetinin, Olga V. Skryabina, Sergey V. Egorov, Valery V. Ryazanov, Alexander A. Golubov, Dimitri Roditchev, and Vasily S. Stolyarov*

Cite This: *J. Phys. Chem. Lett.* 2022, 13, 9221−9231

Read Online

ACCESS | Metrics & More | Article Recommendations | Supporting Information

ABSTRACT: Structural and electronic properties of ultrathin nanocrystals of chalcogenide $Bi_2(Te_x\ Se_{1-x})_3$ were studied. The nanocrystals were formed from the parent compound Bi_2Te_2Se on as-grown and thermally oxidized Si(100) substrates using Ar-assisted physical vapor deposition, resulting in well-faceted single crystals several quintuple layers thick and a few hundreds nanometers large. The chemical composition and structure of the nanocrystals were analyzed by energy-dispersive X-ray spectroscopy, X-ray photoelectron spectroscopy, electron backscattering, and X-ray diffraction. The electron transport through nanocrystals connected to superconducting Nb electrodes demonstrated Josephson behavior, with the predominance of the topological channels [Stolyarov et al. *Commun. Mater.*, **2020**, *1*, 38]. The present paper focuses on the effect of the growth conditions on the morphology, structural, and electronic properties of nanocrystals.

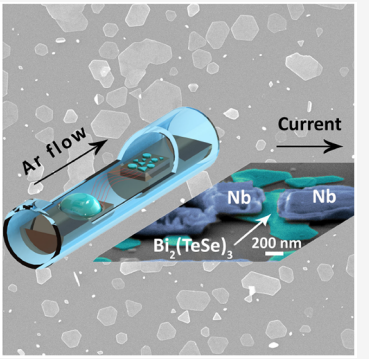

Compound chalcogenides ($Bi_2(Te_xSe_{1-x})_3$, $(Bi_xSb_{1-x})_2Te_3$, etc.) have attracted considerable attention for their thermoelectric characteristics,[1−4] manifestations of topological properties,[5−8] and cancer diagnosis and therapy applications.[9,10] The fabrication of functional devices based on chalcogenides requires control over homogeneity, defects, sizes, the surface-to-bulk conductance ratio,[11] the chemical composition,[12−14] and the chemical potential,[15−17] among many other relevant parameters.

For an effective realization of devices that exploit Dirac phenomena, the electron transport should be dominated by surface states as compared to the bulk. Ideally, the Fermi level should remain within the bulk gap between the valence and conduction bands.[18−22] The ability to fine-tune the Fermi level could result in significant progress in implementations of promising spin transport phenomena[23,24] in addition to gate-tunable[25−27] and Josephson transport devices.[28−30] However, the vast majority of compounds synthesized to date, such as Bi_2Te_3,[31,32] and Bi_2Se_3,[33,34] have a trivial 3D band crossing the Fermi level and are rather thick crystals, both features leading to a detrimentally high bulk conductivity.[35] The search for elaboration methods that address this issue is an important experimental challenge.

Ternary systems Bi_2Se_2Te and Bi_2Te_2Se are promising topological insulators with large surface-to-bulk conductance ratios.[36−43] Nonstoichiometric alloys $Bi_2(Te_xSe_{1-x})_3$[44] have significant spin−orbit coupling strengths, in addition to bulk band gap values and a crystal structure ($R\bar{3}m$, hexagonal) similar to those of Bi_2Se_3 and Bi_2Te_3. Hence, $Bi_2(Te_xSe_{1-x})_3$ are expected to retain their topological properties for the entire range of atomic ratios $0 \leq x \leq 1$, analogous to $(Bi_xSb_{1-x})_2Te_3$.[45,46] Te-rich Bi−Te−Se alloys seem to be preferable for the observation of the topological nature, as they have a high bulk resistivity due to the depleted conduction band.[39,47] Angle-resolved photoemission spectroscopy (ARPES) of Bi_2Te_2Se and $Bi_2Te_{2.5}Se_{0.5}$ showed that only surface states intersected the chemical potential.[35] However, $Bi_2Te_{2.5}Se_{0.5}$ has a smaller bandgap, resulting in a higher bulk conductivity at low temperatures as compared to Bi_2Te_2Se.

Conventionally, ultrathin nanocrystals and films are fabricated by exfoliation from bulk crystals.[48−51] The main limitation of the exfoliation method is that the lateral sizes, thicknesses, and shapes of the flakes are difficult to control.[25,49,52] Moreover, the exfoliation technique is not scalable. High-quality nanocrystals can be fabricated by molecular beam epitaxy (MBE),[53−55] but this technique is complex and expensive. In contrast, the physical vapor deposition (PVD) method offers cost-effective fabrication without the disadvantages inherent to exfoliation.[56−60]

Received: August 28, 2022
Accepted: September 22, 2022
Published: September 28, 2022

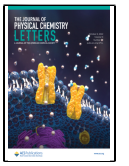

https://doi.org/10.1021/acs.jpclett.2c02664
J. Phys. Chem. Lett. 2022, 13, 9221−9231

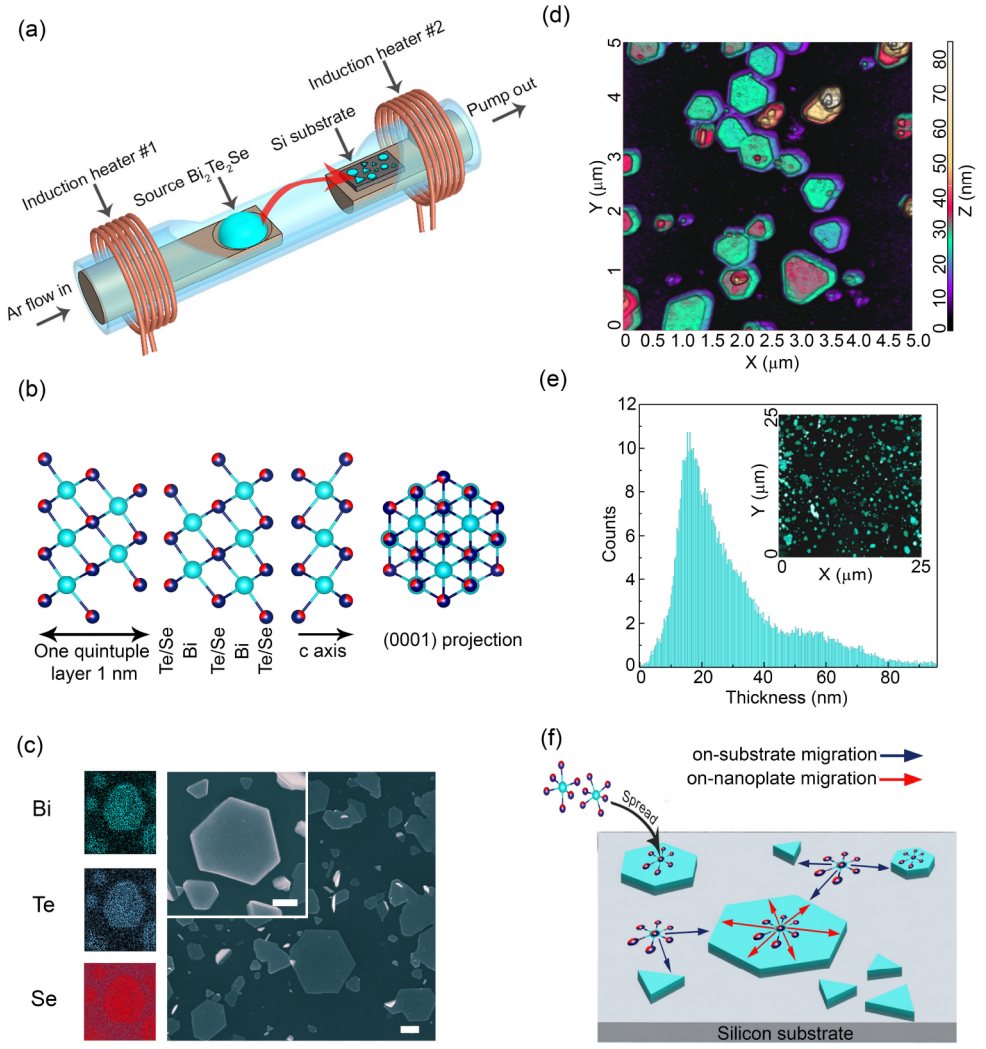

Figure 1. PVD growth of $Bi_2(Te_xSe_{1-x})_3$ nanocrystals. (a) Schematics of the PVD setup and the synthesis process. The source material and the target substrate are placed on holders inside a quartz tube. The holders were remotely heated by inductive heaters. The deposition was assisted by an Ar flow (see details in the text). (b) Crystal structure of $Bi_2(Te_xSe_{1-x})$. (c) SEM image of a selected nanocrystal (the white scale bar corresponds to 1 μm); elemental maps of Bi (green), Te (blue), and Se (red); and an overlaid RGB image recorded using scanning EDX. (d) AFM image of a collection of ultrathin $Bi_2(Te_xSe_{1-x})_3$ nanocrystals demonstrating their flat-top planar hexagonal morphology. (e) Experimental statistics of the AFM-derived distribution of the nanocrystal thicknesses. (Insert) AFM 25 × 25 μm^2 image of the considered area. (f) Schematic illustrations of the nanocrystal growth. The mechanism involves two migration processes, on the substrate surface (blue) and another on the nanocrystal surface (red). The surfaces of the topmost nanocrystals present saturated bonds, while their side surfaces have active dangling bonds that capture incoming atoms.

In this Letter, we describe the PVD growth of ultrathin $Bi_2(Te_xSe_{1-x})_3$ single crystals obtained from a bulk parent Bi_2Te_2Se polycrystal melt. We detail the nanocrystal growth process and the fabrication of planar S−TI−S Josephson junctions.[61] In addition to a detailed discussion of technological aspects, this work provides an analysis of XPS, XRD, EDX, and EBSD data obtained for the synthesized crystals and reports on the transport properties of Nb−$Bi_2(Te_xSe_{1-x})_3$−Nb junctions measured in a wide temperature range.

Nanocrystal synthesis was performed in a home-built PVD reactor (Figure 1(a)) composed of a quartz tube (30 mm in diameter and 120 cm long) and two inductive heaters located outside the tube. The application of induction heaters allows the heating of only the holder while the walls of the reactor remain cold. Such a design has advantages such as reduced precipitation of contaminants on the reactor walls, low energy consumption, and low probability of gas-phase reactions. However, these advantages come at the price using a small number of holders during the synthesis and the thermal stress of the holders that arises if the heating or cooling rates are too high. The deposition material source and the substrate are placed on two special holders, which are located inside the quartz tube reactor 10 cm away from each other. The holders are made of a nickel−copper alloy with a relatively high magnetic permeability and thermal conductivity, two properties important for their effective use in the inductive heaters. To prevent reactions between the holder material and any deposition-process products, the surfaces of the holders were covered with tantalum.

The stoichiometric polycrystal Bi_2Te_2Se melt (Figure 1(b)) was taken as a source. Two types of 5 × 10 mm^2 substrates were used: Si (100) and Si/SiO_2 (300 nm thermal oxide layer) (see Table 1). Substrates were ultrasonically cleaned in acetone and isopropyl alcohol (10 min each) to remove contaminants, rinsed in deionized water, and dried under a nitrogen flow. The temperatures of the source and substrate were T_1 = 500−600

https://doi.org/10.1021/acs.jpclett.2c02664
J. Phys. Chem. Lett. 2022, 13, 9221−9231

Table 1. Summary of the Sample Growth Conditions, Including the Type of Substrate, the Source−Substrate Distance, and Temperatures of the Source (T_1) and the Substrate (T_2)

title	substrate	distance (cm)	T_1 (°C)	T_2 (°C)
S1	Si	5	525	150
S2	Si	5	528	225
S3	Si	5	544	350
S4	Si	10	545	450
S5	Si	15	539	345
S6	Si	10	550	355
S7	Si	10	500	350
S8	Si	10	500	350
S9	SiO_2	10	555	320
S10	SiO_2	10	548	332
S11	SiO_2	10	530	330

°C and T_2 = 70−450 °C, respectively; temperatures were controlled by means of PID regulators acting on the output power of the inductive heaters. Signals from K-type thermocouples embedded in the holders were used as the input for the two PID loops. The precise control of the temperatures is required to provide stable conditions during crystal growth.

Before the growth sequence, the quartz tube was first pumped to 10^{-3} Torr and then flushed with Ar (99.995%). Pure argon gas plays the role of a carrier, which intensifies the transport of the evaporated source material to the colder substrate. During the growth, the pumping speed and the gas flow were adjusted to maintain the constant pressure of 100 Torr in the quartz tube. A typical deposition process takes approximately 15−30 minutes. After that, the heater power was switched off, and both the source and the substrate cooled freely.

In all the cases studied, the growth followed the Vollmer−Weber scenario, due to a significant mismatch between the lattice parameters of Si/SiO_2 and those of $Bi_2(Te_xSe_{1-x})_3$.[62] Synthesized nanocrystals have good adhesion to the substrate; it is difficult to remove them even with an organic solvent in an ultrasonic bath. By varying the source and substrate temperatures, the source−substrate distance, and the growth duration, one can change the morphology of the deposited structures. For the parameters mentioned above, we obtained thin (10−40 nm) nanocrystals with lateral sizes ranging from 100 nm to ∼5 μm; these parameters were measured using scanning electron microscopy (SEM) (see Supplementary Figure 1) and by atomic force microscopy (AFM) (Figure 1(d and e)).

The fabricated samples were characterized by electron backscatter diffraction (EBSD) on a ZEISS Gemini system

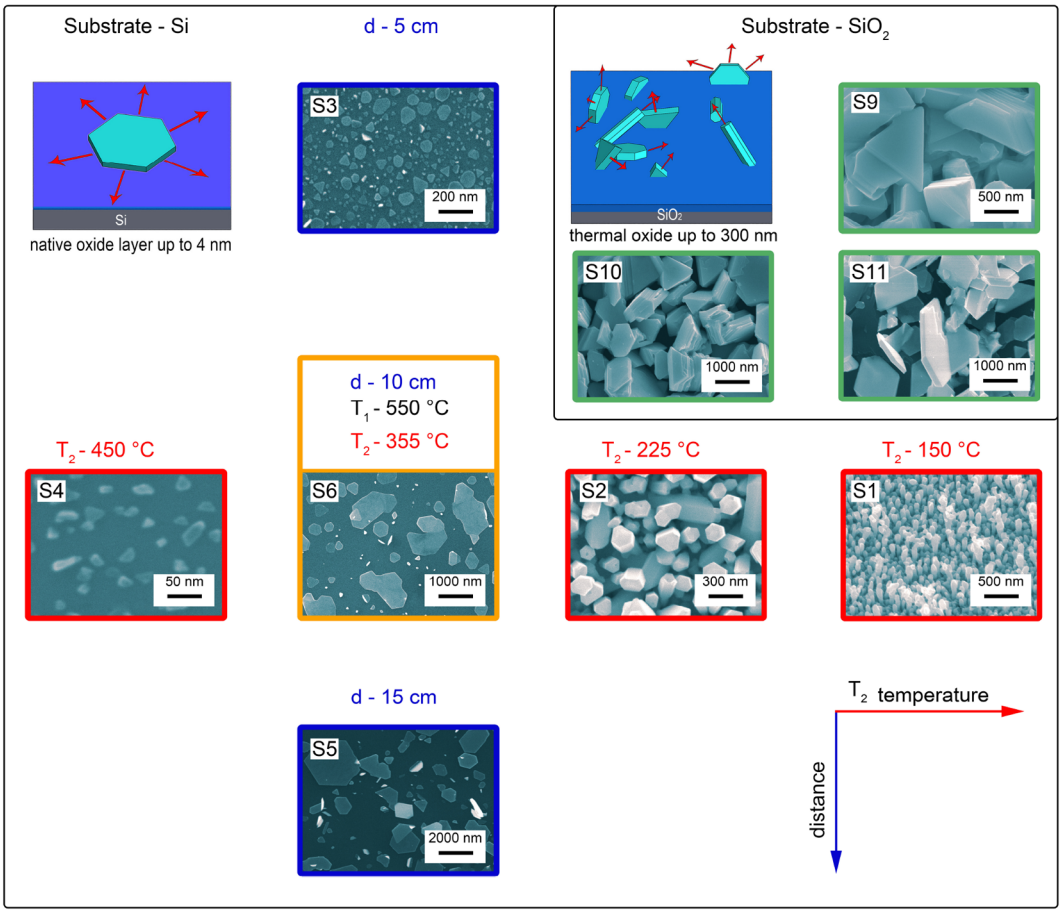

Figure 2. Summary of the samples grown on native Si substrates (left and bottom) and thermally oxidized Si (right-top). The obtained $Bi_2(Te_xSe_{1-x})_3$ samples are represented by their SEM images placed on the substrate temperature plane (T_2, horizontal axis) vs the source−substrate distance (d, vertical axis). The growth processes are different on Si(100) and SiO_2/Si, as schematized by the two drawings. The set of parameters at which very flat well-faceted islands were obtained is marked by an orange frame.

https://doi.org/10.1021/acs.jpclett.2c02664
J. Phys. Chem. Lett. 2022, 13, 9221−9231

equipped with an EDX spectrometer, which revealed the characteristic features of the as-grown $Bi_2(Te_xSe_{1-x})_3$ nanocrystals. The structural orientation of the samples was investigated by XRD using both $\theta-2\theta$ and 4φ scans on a Rigaku SmartLab SE system. The X-ray generator was operated at 50 kV and 100 mA. Surface morphologies were analyzed using a Jeol JSM 7001FA field-emission SEM (Figure 1(c)). The AFM images were obtained in a hybrid mode on the NT-MDT next 2 microscope to measure the nanocrystal thickness (Figure 1(d and e)). XPS analysis was performed using a Kratos AXIS Ultra DLD spectrometer with a delay line detector (DLD) and a depth resolution of 2−8 nm.

For transport measurements, submicrometer-scale planar Nb−$Bi_2(Te_xSe_{1-x})_3$−Nb junctions were created by contacting deposited nanocrystals with Nb electrodes. Each planar junction consists of two superconducting Nb electrodes separated by a 100−150 nm gap and a single nanocrystal between them that acts as a weak link. The fabrication recipe included two steps of lift-off electron beam lithography (EBL), and Nb film deposition was performed after each EBL step.

The first step of the two-step EBL procedure consists of the creation of a marker network as well as of the array of small Nb dots. After this step, SEM was used to find and chose locations where two neighboring Nb dots contacted the same $Bi_2(Te_xSe_{1-x})_3$ nanocrystal, thus forming a planar junction. At the second EBL step, each selected junction was wired to large metallic pads, thus enabling transport measurements.

To perform the EBL, a substrate containing the nanocrystals on its surface was covered with a 250 nm thick layer of the e-beam resist PMMA 950 K and baked for several hours at 60 °C. To pattern the masks, we used a JEOL 7001f SEM equipped with an EBL module. The necessary dose in our case was 400 $\mu C/cm^2$. We used a mixture of one part MIBK and three parts IPA to develop the e-beam pattern and clean IPA as a stopper. After the development, the mask was dried in N_2 gas. The consequent Nb film deposition was performed via magnetron sputtering in an Ar environment. The base vacuum was not lower than 4×10^{-9} Torr, and during the process the pressure was 7×10^{-3} Torr. Short-time ion milling was applied to remove resist residues at the contact locations and improve the transparency of the Nb−$Bi_2(Te_xSe_{1-x})_3$ interfaces. The argon discharge parameters were as follows: power of 60 W, bias voltage of 480 V, Ar flow of 10 sccm, and pressure of about 1×10^{-2} mbar. The metallic structure was lifted in hot acetone, and it took several hours to remove all the PMMA residue. Subsequently, an IPA rinse and N_2 flow drying were applied.

The evolution of the electrical resistance of the junctions with temperature was measured in a quasi-four-probe configuration in the range of 1.2−300 K. The samples were placed in an insert of a liquid He-4 cryostat. A Keithley 6220 current source was used as a current source, and the voltage drop across the junctions was recorded by a Keithley 2182a. Special care was taken to reduce the influence of the RF noise. For each current and voltage lead, separated twisted pairs were used; each pair was equipped with a low-temperature low-pass RC filter with a 250 Hz cutoff frequency.

The growth of the ultrathin nanocrystals follows the vapor−solid mechanism because of the anisotropy of the bonding forces in the lattices of Bi_2Se_3 and Bi_2Te_3. Surface defects of the Si substrate, dislocations, or chemical inhomogeneities (impurities) are the expected starting points of the nucleation process. The *c*-axes of the nuclei are oriented normally to the substrate surface. The anisotropic nature of the crystal bonds causes the diffusion of new atoms on the top surface. These atoms are formed by chemically saturated Se atoms, which leads them to join dangling bonds on the edges of the crystal (see Figure 1(f)). Therefore, under particular conditions, the lateral dimensions grow much faster than the vertical (thickness) dimension.

The morphology of the synthesized nanocrystals strongly depends on several factors: (i) the substrate material, (ii) the substrate temperature T_2, and (iii) the source−substrate distance (see Table 1). Figure 2 shows the consequent changes in the sample microstructure when different conditions are changed (and the other parameters are kept constant).

(i) Though a Si substrate still has a thin native oxide layer (up to 4 nm[63]), atoms of the source material may presumably migrate more easily there than on the surface of a thicker 300 nm thermal oxide layer of a Si/SiO_2 substrate, which has dangling bonds and a signigicantly rough surface. The role of the migration on the Si surface in nanocrystal growth may be further confirmed by a correlation between the lateral sizes of the nanocrystals and the distance between neighboring nanocrystals. Nanocrystals grown on a silicon substrate have a hexagonal planar structure, with the *c*-axis normal to the substrate surface. During the deposition process nanocrystals tend to grow in lateral sizes rather than in height. The wider nanocrystals coalesce with each other. Schematics of the growth process and SEM images of nanocrystals on a Si substrate are shown in the insets in Figure 2 (samples S1−S8). The reader can find more SEM images in the Supporting Information. In contrast, nanocrystals on a Si/SiO_2 substrate did not have a preferential growth direction and were located randomly. A growth sketch and SEM images are depicted in the inset in Figure 2 (the upper-right corner, samples S9−S11). One can obtain not only thin flat nanocrystals but also conglomerates of nanocrystals. That might be explained by the amorphous nature of SiO_2, which, nevertheless, does not affect the crystal symmetry of deposited $Bi_2(Te_xSe_{1-x})_3$.

(ii) At relatively low substrate temperature (T_2 = 70 °C), the mobility of atoms deposited on Si is low, so they form an amorphous film. At the substrate temperature of T_2 = 150 °C (sample S1), the surface is uniformly covered with the amorphous film and whiskers protrude from the surface. This indicates that a large temperature gradient is undesirable for growth. At T_2 = 225 °C (sample S2), the growth of transverse whiskers starts. At T_2 = 355 °C (sample S6), the nanocrystals have a planar triangular or hexagonal morphology with lateral dimensions that extend up to a few micrometers. The nanocrystal thickness distribution for this sample is shown in Figure 1(e). At temperatures of 450 °C (sample S4) and higher, atoms of Bi, Se, and Te are close to the evaporation point and therefore to the breaking of van der Waals bonds between the quintuple layers. Only small objects can be observed at this temperature.

(iii) Nanocrystals with different sizes can be obtained by changing the distance between the source and the Si substrate. When the Si substrate is placed as close as 5 cm to the source (sample S3, Figure 3(a)), the

https://doi.org/10.1021/acs.jpclett.2c02664
J. Phys. Chem. Lett. 2022, 13, 9221−9231

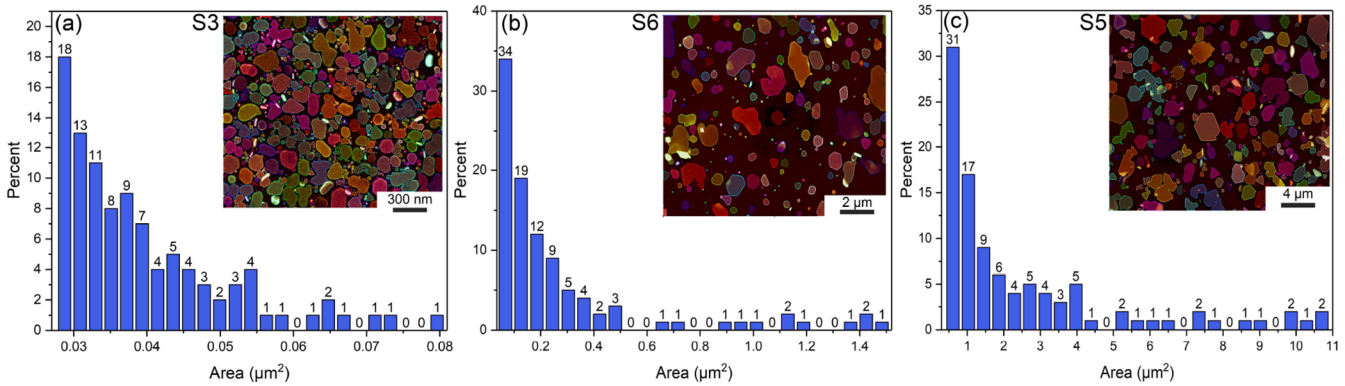

Figure 3. Area distributions for the grown nanocrystals and SEM images of the surface microstructure (single nanocrystals are depicted in different colors for clarity). (a) Sample S3 with a 5 cm distance between the receiving substrate and the source material, single-crystal area up to 0.082 μm^2. (b) Sample S6 with a 10 cm between the receiving substrate and the source material, nanocrystals from 0.082 to 1.47 μm^2. (c) Sample S5 with a 15 cm distance between the receiving substrate and the source material, larger nanocrystals with sizes up to 11 μm^2. Growth parameters of the described samples can be found in Table 1.

synthesized nanocrystals have an area not larger than 0.082 μm^2, with an average value of 0.040 μm^2. The increase of the source−substrate distance results in the decrease of the nuclei number, but the average area of the nanocrystals increases. The nanocrystals shown on a SEM image in Figure 3(b) (10 cm gap) have an area distribution up to 1.47 μm^2 (Figure 3(b)), with an average area of 0.28 μm^2. Finally, a 15 cm (sample S5) gap between the substrate and the source (Figure 3(c)) causes the growth of nanocrystals with micrometer sizes up to 11 μm^2 (2.51 μm^2 average). Therefore, the lateral size distribution of the nanocrystals depends on the distance between the source and the substrate, and the average nanocrystal's areas in the range from 0.01 to 10 μm^2.

We performed XPS measurements on as-deposited samples and after Ar plasma etching (120 and 240 s). Initially, the spectra indicate the presence of Bi−Te atoms (Bi 4f 7/2, 159.6 eV; Te 3d 5/2, 576.4 eV), oxygen atoms (O 1s, 532.6 eV), and carbon contamination (C 1s, 285.2 eV) (the black curve in Figure 4(a)). The peaks corresponding to Te and Bi are doubled due to oxide signals of Te−O (Te 3d 5/2, 587.2 eV) (Figure 4(b)) and Bi−O (Bi 4f 7/2, 164.8 eV) (Figure 4(c)), which disappear after 120 s of Ar plasma etching (blue curve on Figure 4(a)). Longer Ar etching of 240 s leads to the complete removal of the nanocrystals, so the Bi−Te peaks vanish (the magenta curve in Figure 4(a)) and the only signals that remain are coming from the substrate (Si 2p, 99.2 eV; Si 2s, 150.8 eV). The influence of the Ar plasma on the nanocrystals can be clearly seen in the SEM image in Figure 4(d). Therefore, the preferred etching parameters prior to XPS analysis, which allow the removal of surface oxides and contamination without damaging the nanocrystals, are as follows: etching time of 120 s, Ar pressure of 1.6×10^{-6} mbar, acceleration voltage of 4 kV, and average etching rate of 0.05−0.10 nm/s for nanocrystals with a thickness of approximately 20 nm.

The crystalline structure and orientation of the ultrathin $Bi_2(Te_xSe_{1-x})_3$ nanocrystals were investigated by X-ray diffraction using a $\theta-2\theta$ scan (Figure 4(e)). The XRD patterns can be steadily indexed in the Bi_2Te_2Se structure (ICDD card no. 01-089-2006, 166; $R\bar{3}m$, hexagonal) see Table 2. The XRD pattern revealed that the $Bi_2(Te_xSe_{1-x})_3$ samples crystallized into a single hexagonal phase, with the predominant peaks indexed into the (001) lattice plane. The three high-intensity peaks in each spectrum can be fully indexed with the crystallographic planes (006), (015), and (1010), respectively, in the hexagonal phase $R\bar{3}m$. Analysis of the relative intensity of the lines shows the presence of the weak orientation of type (001). The lattice parameters were found to be $a = b = 4.319$ Å and $c = 30.018$ Å. All these obtained values are in agreement with the reported parameters.[64,65] Furthermore, it shows that the unit cell of the sample is more contracted, especially along the c-axis, due to the shortened quintuple layer (QL) Te/Se−Bi−Te/Se−Bi−Te/Se caused by the substitution of a smaller Se at the larger Te position.

The chemical composition of the synthesized nanocrystals was also proven by the unit cell volume $V = 486.03(7)$ Å^3, which was measured by WPPF analysis (see Table 2) and was very close to the value of 486.1 Å^3 expected from Vegard's law (see Supplementary Figure 2) $V = V_A^0(1 - Y) + V_B^0(Y)$, where V is the unit cell volume of the material studied, $V_A^0 = 450.5$ Å^3 is the unit cell volume of Bi_2Se_2Te, $V_B^0 = 508.4$ Å^3 is the unit cell volume of Bi_2Te_3, and Y accounts for the relative concentration of Te and Se.[66] The values of the unit cell volumes were taken from PDF-2 (ICDD) database.

To characterize the elemental composition of the synthesized nanocrystals, energy-dispersive X-ray spectroscopy (SEM and EDX) was used. Table 3 provides the results of the EDX analysis performed on the nanocrystals S3, S5, S6, S7, S8, and S9 and the source material S. For a reliable comparison, the composition of the source material and the elemental content were measured and averaged over 20 times. The errors presented are estimated as a combination of a standard error and the ∼2% uncertainty of the EDX measurements. The composition of the source material corresponds to the stoichiometric Bi_2Te_2Se compound. High-energy (10 keV) electrons penetrate into the sample up to a depth of 0.5 μm (the nanocrystal thickness is <100 nm), hence the raw EDX spectra acquired on all nanocrystals demonstrate a significant amount of the Si substrate material. The raw EDX spectra were normalized with respect to the Bi peaks (2.51 keV) for comparison. The spectra from the nanocrystals were decomposed to the Bi_2Te_3 and Bi_2Se_3 reference spectra to determine the atomic ratio between Te and Se. All measured nanocrystals show a similar elemental content, which is the

https://doi.org/10.1021/acs.jpclett.2c02664
J. Phys. Chem. Lett. 2022, 13, 9221−9231

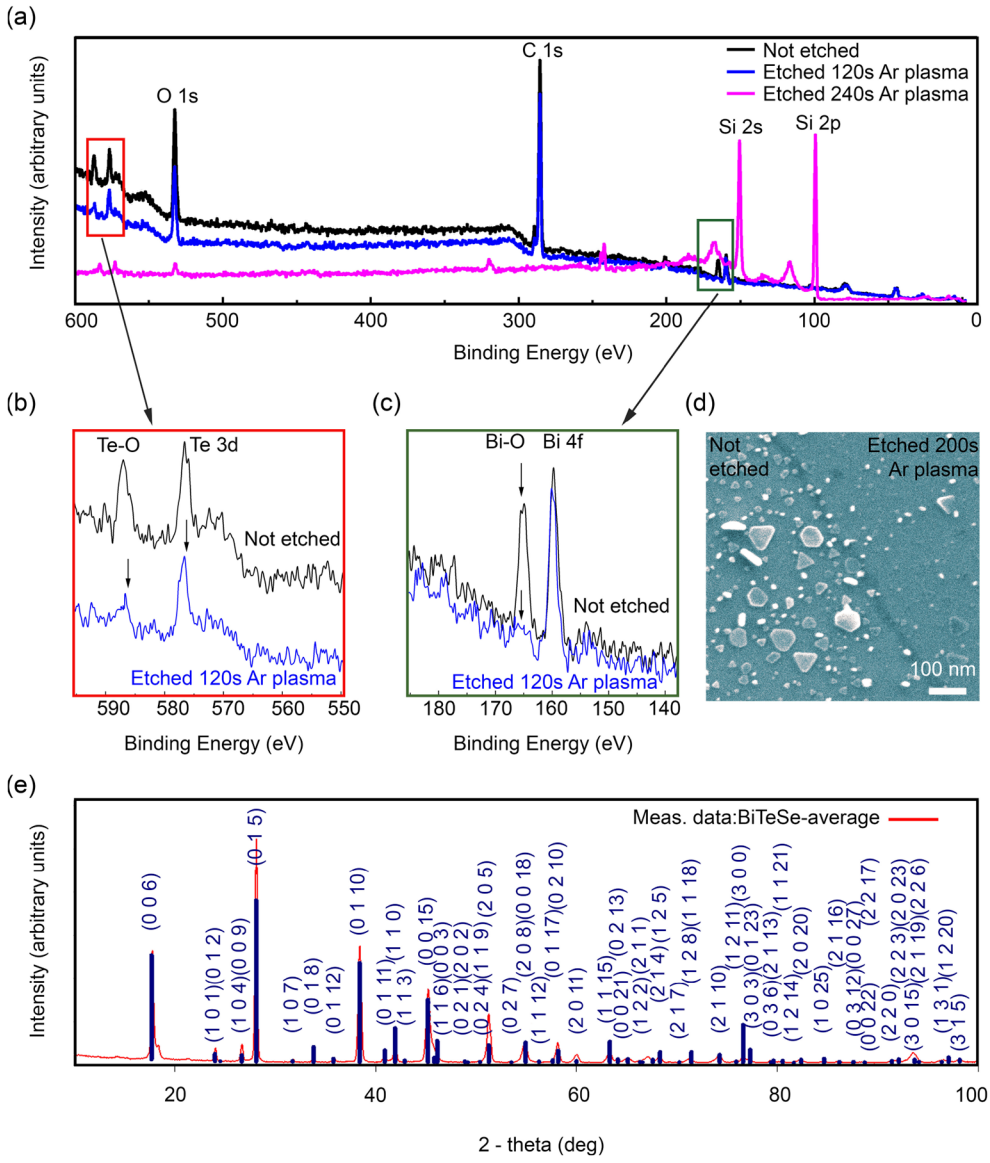

Figure 4. Component and crystalline orientation analysis of the $Bi_2(Te_xSe_{1-x})_3$ nanocrystals. (a) XPS spectra of $Bi_2(Te_xSe_{1-x})_3$ nanocrystals on a Si substrate etched with Ar plasma for different durations. The color code is as follows: no etching (black), 120 s of etching (blue), and 240 s of etching (magenta). (b) The part of the XPS spectra with the Te and Te−O peaks. The color code is as follows: no etching (black) and 120 s of Ar plasma etching (blue). (c) The part of the XPS spectra with the Bi and Bi−O peaks. The color code is as follows: no etching (black) and 120 s of Ar plasma etching (blue). (d) SEM image of the sample surface before and after 200 s of Ar plasma etching. (e) Representative XRD pattern recorded for a thick polycrystal $Bi_2(Te_xSe_{1-x})_3$ film grown on a Si (100) substrate. The peaks corresponding to diffraction on different atomic planes are labeled with (*hkl*) indices.

Table 2. Structural Parameters Obtained from the Whole Powder Pattern Fitting (WPPF) Analysis

phase name	formula	space group	*a* (Å)	*b* (Å)	*c* (Å)	*α*	*β*	*γ*	*V* (Å^3)
kawazulite	Bi_2Te_2Se	166:$R\bar{3}m$, hexagonal	4.319(4)	4.319(4)	30.081(3)	90.0°	90.0°	120.0°	486.03(7)

stoichiometry $Bi_2(Te_xSe_{1-x})_3$. A few samples produced EDX spectra that give the expected ratio, as shown in Supplementary Figure 3.

The elemental maps of Bi, Te, and Se acquired from the EDX scan are presented in Figure 1(d). The observed elemental distribution indicates that Bi and Te atoms are fairly uniformly distributed inside a single nanocrystal without obvious precipitates. As in the case of a point EDX analysis, the intense signal of the thick Si substrate significantly reduces the Se signal, which does not allow the unambiguous definition of the spatial distribution of Se inside a single nanocrystal.

A possible explanation of a lower contrast in the EDX scan for Se is the passivation of the entire sample surface with Se atoms, as Se has the lowest melting temperature among the materials in the chemical composition of the nanocrystals. Such a layer of Se can also prevent the sample from oxidation in atmospheric air.[67]

To investigate the crystallinity and the orientation of the $Bi_2(Te_xSe_{1-x})_3$ nanocrystals grown at 350 °C on the Si

https://doi.org/10.1021/acs.jpclett.2c02664
J. Phys. Chem. Lett. 2022, 13, 9221−9231

Table 3. Results of the EDX Analysis[a]

title	Bi (at. %)	X_{EDX} (average)	formula
S	39.22 ± 1.44	0.67 ± 0.012	$Bi_2Te_{2.01}Se_{0.99}$
S3	38.15 ± 1.53	0.81 ± 0.015	$Bi_2Te_{2.43}Se_{0.57}$
S5	41.43 ± 1.91	0.59 ± 0.017	$Bi_2Te_{1.77}Se_{1.23}$
S6	39.24 ± 1.51	0.77 ± 0.009	$Bi_2Te_{2.31}Se_{0.69}$
S7	43.55 ± 2.36	0.79 ± 0.011	$Bi_2Te_{2.37}Se_{0.63}$
S8	53.07 ± 3.2	0.85 ± 0.007	$Bi_2Te_{2.57}Se_{0.43}$
S9	38.71 ± 2.54	0.74 ± 0.013	$Bi_2Te_{2.22}Se_{0.78}$

[a]The atomic composition of the source material S and single nanocrystals. The raw EDX spectra were normalized with respect to the Bi peaks (2.51 keV) for comparison. The spectra of the ternary nanocrystals were decomposed to the Bi_2Te_3 and Bi_2Se_3 reference spectra to determine the atomic ratio between Te and Se.

substrate, an EBSD analysis was performed on a single nanocrystal (the corresponding SEM image is shown in Supplementary Figure 4a). The EBSD data are consistent with the XRD data and confirm that the crystal structure matches that of the hexagonal phase of $Bi_2(Te_xSe_{1-x})_3$ in the PDF-2 database as follows: the hexagonal space group $R\bar{3}m$ (166), $a = b = 0.430$ nm, $c = 2.97$ nm, $\alpha = \beta = 90°$, and $\gamma = 120°$. The crystallographic orientation mapping using the inverse pole figure (IPF) color code along with the *x*-, *y*-, and *z*-directions are shown in Supplementary Figure 4b–e and f–i for the $Bi_2(Te_xSe_{1-x})_3$ nanocrystal and the Si substrate, respectively, where the perfectly homogeneous color is found in each. This indicates that the crystallinity of our $Bi_2(Te_xSe_{1-x})_3$ nanocrystals is nearly perfect.

For the investigated $Bi_2(Te_xSe_{1-x})_3$ nanocrystal, the IPF along the *x*-, *y*-, and *z*-directions shown in Supplementary Figure 4j indicate that the out-of-plane orientation is ⟨0001⟩, and the in-plane orientations are ⟨1120⟩ and ⟨1010⟩. The IPF along the *x*-, *y*-, and *z*-directions for the Si substrate is shown in Supplementary Figure 4k. A comparative analysis of the IPF data for the nanocrystal and the substrate (Supplementary Figure 4b–e and f–k, respectively) reveals that the alignment between the $Bi_2(Te_xSe_{1-x})_3$ nanocrystal and the Si substrate is (0001) $Bi_2(Te_xSe_{1-x})_3$ ∥ (001) Si and [1120] $Bi_2(Te_xSe_{1-x})_3$ ∥ [101] Si.

The electronic properties of three submicrometer-scale planar Nb–$Bi_2Te_{2.43}Se_{0.57}$–Nb junctions J1–J3 (see Figure 5(a)) were studied. The weak-link regions have a length of $L_n \approx 130$ nm and different widths W_n from 154 to 211 nm (see Table 4). A systematic evolution of the temperature-dependent electrical resistance 6R is presented in Figures 5(b and c) for different nanocrystal thicknesses.

Resistances of Nb–$Bi_2Te_{2.43}Se_{0.57}$–Nb junctions at room temperature were in the range of 1.5–2.2 kΩ. Measurements were performed in a quasi-four-probe configuration, so the resistance measured above the critical temperature T_c includes the resistance of the nanocrystal itself, those of the two Nb–$Bi_2Te_{2.43}Se_{0.57}$ interfaces, and those of the two Nb wires. The wires have a room-temperature resistance of approximately 100 Ω and a residual resistance ratio value RRR = 3. A typical $R(T)$ dependence for Nb used in the experiment can be seen in Supplementary Figure 5. Therefore, the low-temperature resistance of the Nb leads of ∼30 Ω was much less than the nanocrystal resistance, and R_n (see Table 4) measured just above T_c was as the nanocrystal resistance. This allows us to estimate the thickness of the nanocrystal using the electrical resistivity ρ taken from the work.[35]

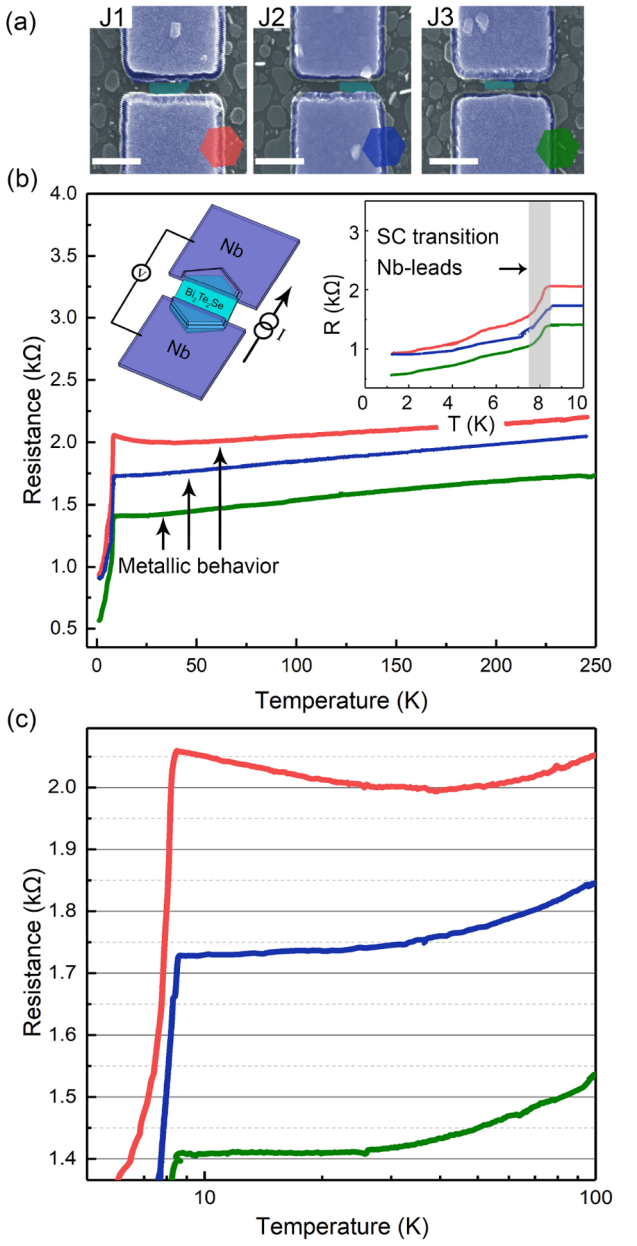

Figure 5. SEM images of Nb–$Bi_2Te_{2.43}Se_{0.57}$–Nb junctions and their $R(T)$ characteristics. (a) SEM images of the submicrometer-scale junctions J1–J3. All junctions have a length of separation between Nb leads of $L_n \approx 130$ nm (see the exact sizes in Table 4). The colors shown in the bottom-right corner of each SEM image correspond to those on the $R(T)$ graphs. (b) The temperature dependence of the device resistances from 1.2 to 250 K. A schematic illustration of the measurements used in this work is shown in the top-left inset. The region of the superconducting transition is shown as a gray band in the top -ight inset. (c) The ln *T* dependence of the resistance. The nanocrystal J1 with the minimal thickness displays metallic behavior at high temperatures but shows a localization-related "bad metal" behavior at low temperatures.

In general, junctions through the nanocrystals (J1–J3) clearly demonstrated a metallic tendency ($dR/dT > 0$) from 300 down to 40 K. The resistances of these samples decrease almost linearly as a result of electron–phonon scattering of the bulk carriers. Below 40 K, the samples demonstrate different behaviors. The resistance of J1 has a slight 50 Ω kink before

https://doi.org/10.1021/acs.jpclett.2c02664
J. Phys. Chem. Lett. 2022, 13, 9221–9231

Table 4. Measured Junction Parameters: Distance between the Nb Electrodes L_n, Width of the Nanocrystal W_n, Junction Normal Resistance R_n, and Nanocrystal Thickness d[a]

title	L_n (nm)	W_n (nm)	R_n (Ω)	d (nm)
J1	125 ± 5	211 ± 10	2057	10
J2	129 ± 5	193 ± 10	1727	15
J3	127 ± 5	154 ± 10	1430	20

[a]Calculated from the resistance and consistent with the AFM data.

the superconducting transition, while the resistances of the other two samples J2 and J3 continue to decrease monotonically. A more clear comparison of the resistance is shown in the "semi-ln" plot (Figure 5(c)). This distinction can be explained by manifestations of surface-state resistance against the background of freezing bulk carriers in topological insulators, which is more apparent in thinner samples.[67,68]

The superconducting transition of the Nb lead regions overlapped by $Bi_2Te_{2.43}Se_{0.57}$ nanocrystal takes place lower $T_c^{Nb} \approx 8.2$ K, as shown in the inset of Figure 5(b). Below the Nb critical temperature, there is a broadened transition to the superconducting state. The transition has two parts: the first one is related to the overlapping regions, and the second one, occuring at yet lower temperatures, is the transition of the weak links to the superconducting state by proximity.

To summarize, we synthesized ultrathin nanocrystals of $Bi_2(Te_xSe_{1-x})_3$ using a PVD reactor with an improved design based on induction heaters. Careful control of the synthesis parameters (temperatures of the substrate and the source, the distance between the substrate and the source, the duration of the deposition process, and the type of substrate) allowed us to find the optimal conditions for growing ultrathin single nanocrystals. These have a smooth surface with a metallic reflection, a planar triangular or hexagonal morphology, a thickness of 10−20 nm with lateral sizes ranging from 100 nm to ∼5 μm, and a layered structure. Nanocrystals synthesized on an as-grown Si(100) substrate demonstrated a planar type of growth, while those synthesized on a thermally oxidized Si/SiO_2 substrate did not demonstrate a preferential growth direction.

The XRD, XPS, EDX, and EBSD data confirmed that the $R\bar{3}m$ hexagonal crystal lattice structure and the chemical composition match those of $Bi_2(Te_xSe_{1-x})_3$. The study of the same sample through different complementary methods revealed a clear relationship among the topography, crystallographic structure, and chemical composition of the samples.

Preliminary low-temperature measurements of nanocrystal-based structures showed their metallic behavior throughout the temperature range of 40−100 K. In the low-temperature limit, the resistance of the thinnest sample increases, presumably as a result of the localization of surface-state carriers. The effect vanishes in thicker samples, due to the increased defectiveness.

The main advantage of the demonstrated PVD method is the possibility to vary the atomic composition of the synthesized $Bi_2(Te_xSe_{1-x})_3$ crystals in the entire range of atomic ratios $0 \le x \le 1$ (see Table 3). The resulting composition is defined by the synthesis parameters; however, the precise connection among them is not yet known. The development of a technique allowing the synthesis of crystals of any arbitrary composition and thus precise tuning of the Fermi level still represents a big challenge. We hope that our work will facilitate the study of topological insulators and TI-based electronic and spintronic devices such as hybrid superconducting Josephson devices.

■ ASSOCIATED CONTENT

Supporting Information

The Supporting Information is available free of charge at https://pubs.acs.org/doi/10.1021/acs.jpclett.2c02664.

SEM image of tilted Nb−$Bi_2Te_{2.43}Se_{0.57}$−Nb junctions, dependence of unit cell volume on the substitution ratio of Se, EDX and EBSD spectra of the nanocrystals, R(T) dependence of the Nb film, and SEM images of samples S7 and S8 (PDF)

■ AUTHOR INFORMATION

Corresponding Author

Vasily S. Stolyarov − *Center for Advanced Mesoscience and Nanotechnology, Moscow Institute of Physics and Technology, Dolgoprudny, Moscow Region 141700, Russia; Dukhov Research Institute of Automatics (VNIIA), Moscow 127055, Russia; National University of Science and Technology MISIS, Moscow 119049, Russia;* orcid.org/0000-0002-5317-0818; Email: stolyarov.vs@phystech.edu

Authors

Dmitry S. Yakovlev − *Center for Advanced Mesoscience and Nanotechnology, Moscow Institute of Physics and Technology, Dolgoprudny, Moscow Region 141700, Russia; Russian Quantum Center, Skolkovo, Moscow Region 143025, Russia;* orcid.org/0000-0002-6894-2139

Dmitry S. Lvov − *Institute of Solid State Physics RAS, Chernogolovka, Moscow Region 142432, Russia*

Olga V. Emelyanova − *National Research Nuclear University MEPhI, Moscow 115409, Russia;* Present Address: Center for Energy Science and Technology, Skolkovo Institute of Science and Technology, Moscow, Russia

Pave S. Dzhumaev − *National Research Nuclear University MEPhI, Moscow 115409, Russia*

Igor V. Shchetinin − *National University of Science and Technology MISIS, Moscow 119049, Russia*

Olga V. Skryabina − *Center for Advanced Mesoscience and Nanotechnology, Moscow Institute of Physics and Technology, Dolgoprudny, Moscow Region 141700, Russia; Institute of Solid State Physics RAS, Chernogolovka, Moscow Region 142432, Russia; National University of Science and Technology MISIS, Moscow 119049, Russia;* orcid.org/0000-0003-1863-4733

Sergey V. Egorov − *Russian Quantum Center, Skolkovo, Moscow Region 143025, Russia; Institute of Solid State Physics RAS, Chernogolovka, Moscow Region 142432, Russia*

Valery V. Ryazanov − *Russian Quantum Center, Skolkovo, Moscow Region 143025, Russia; Institute of Solid State Physics RAS, Chernogolovka, Moscow Region 142432, Russia; National University of Science and Technology MISIS, Moscow 119049, Russia*

Alexander A. Golubov − *Faculty of Science and Technology, MESA+ Institute of Nanotechnology, Enschede 7500 AE, The Netherlands*

Dimitri Roditchev − *Laboratoire de Physique et d'Étude des Matériaux (LPEM), UMR-8213, ESPCI Paris, PSL Research University, CNRS, Sorbonne Université, Paris 75005, France*

Complete contact information is available at:

https://doi.org/10.1021/acs.jpclett.2c02664
J. Phys. Chem. Lett. 2022, 13, 9221−9231

https://pubs.acs.org/10.1021/acs.jpclett.2c02664

Author Contributions

V.S.S. suggested the idea for the experiment. V.S.S supervised the experiments. D.S.Y and V.S.S grew the nanocrystals. V.S.S. and O.V.S. performed e-beam lithography and thin film deposition. O.V.S, D.S.L, V.S.S, and D.S.Y performed low-temperature experiments. O.V.E, P.S.D, and I.V.S analyzed the chemical compositions. D.S.Y, D.S.L, V.V.R., A.A.G., V.S.S., and D.R. wrote the manuscript with essential contributions from other authors.

Notes

The authors declare no competing financial interest.

■ ACKNOWLEDGMENTS

We gratefully acknowledge valuable discussions with S. Dizhur. We thank D. Baranov and R. Morari for their technical support. The reported study was funded by RFBR, project number 20-32-90060. The transport measurements were carried out with the support of the RSF (21-72-00140). The work of V.V.R and S.V.E. was supported by Rosatom (contract no. 868-1.3-15/15-2021).

■ REFERENCES

(1) Scheele, M.; Oeschler, N.; Meier, K.; Kornowski, A.; Klinke, C.; Weller, H. Synthesis and Thermoelectric Characterization of Bi_2Te_3 Nanoparticles. *Adv. Funct. Mater.* **2009**, *19*, 3476−3483.

(2) Beretta, D.; Neophytou, N.; Hodges, J. M.; Kanatzidis, M. G.; Narducci, D.; Martin-Gonzalez, M.; Beekman, M.; Balke, B.; Cerretti, G.; Tremel, W.; et al. Thermoelectrics: From History, a Window to the Future. *Materials Science and Engineering: R: Reports* **2019**, *138*, 100501.

(3) Soni, A.; Yanyuan, Z.; Ligen, Y.; Aik, M. K. K.; Dresselhaus, M. S.; Xiong, Q. Enhanced Thermoelectric Properties of Solution Grown $Bi_2Te_{(3-x)}Se_x$ Nanoplatelet Composites. *Nano Lett.* **2012**, *12*, 1203−1209.

(4) Min, Y.; Park, G.; Kim, B.; Giri, A.; Zeng, J.; Roh, J. W.; Kim, S. I.; Lee, K. H.; Jeong, U. Synthesis of Multishell Nanoplates by Consecutive Epitaxial Growth of Bi_2Se_3 and Bi_2Te_3 Nanoplates and Enhanced Thermoelectric Properties. *ACS Nano* **2015**, *9*, 6843−6853.

(5) Cha, J. J.; Koski, K. J.; Cui, Y. Topological Insulator Nanostructures. *Phys. Status Solidi RRL* **2013**, *7*, 15−25.

(6) Culcer, D.; Cem Keser, A.; Li, Y.; Tkachov, G. Transport in Two-Dimensional Topological Materials: Recent Developments in Experiment and Theory. *2D Materials* **2020**, *7*, 022007.

(7) Kou, L.; Ma, Y.; Sun, Z.; Heine, T.; Chen, C. Two-Dimensional Topological Insulators: Progress and Prospects. *journal of physical chemistry letters* **2017**, *8*, 1905−1919.

(8) Stolyarov, V.; Sheina, V.; Khokhlov, D.; Vlaic, S.; Pons, S.; Aubin, H.; Akzyanov, R.; Vasenko, A.; Menshchikova, T.; Chulkov, E.; et al. Disorder-Promoted Splitting in Quasiparticle Interference at Nesting Vectors. *J. Phys. Chem. Lett.* **2021**, *12*, 3127−3134.

(9) Zhang, X.-D.; Chen, J.; Min, Y.; Park, G. B.; Shen, X.; Song, S.-S.; Sun, Y.-M.; Wang, H.; Long, W.; Xie, J.; et al. Metabolizable Bi_2Se_3 Nanoplates: Biodistribution, Toxicity, and Uses for Cancer Radiation Therapy and Imaging. *Adv. Funct. Mater.* **2014**, *24*, 1718−1729.

(10) Chen, Y.; Wu, Y.; Sun, B.; Liu, S.; Liu, H. Two-Dimensional Nanomaterials for Cancer Nanotheranostics. *Small* **2017**, *13*, 1603446.

(11) Chen, C.-Z.; Xie, Y.-M.; Liu, J.; Lee, P. A.; Law, K. T. Quasi-One-Dimensional Quantum Anomalous Hall Systems as New Platforms for Scalable Topological Quantum Computation. *Phys. Rev. B* **2018**, *97*, 104504.

(12) Shikin, A.; Estyunin, D.; Surnin, Y. I.; Koroleva, A.; Shevchenko, E.; Kokh, K.; Tereshchenko, O.; Kumar, S.; Schwier, E.; Shimada, K.; et al. Dirac Gap Opening and Dirac-Fermion-Mediated Magnetic Coupling in Antiferromagnetic Gd-doped Topological Insulators and Their Manipulation by Synchrotron Radiation. *Sci. Rep.* **2019**, *9*, 4813.

(13) Chang, C.-Z.; Zhao, W.; Kim, D. Y.; Zhang, H.; Assaf, B. A.; Heiman, D.; Zhang, S.-C.; Liu, C.; Chan, M. H.; Moodera, J. S. High-Precision Realization of Robust Quantum Anomalous Hall State in a Hard Ferromagnetic Topological Insulator. *Nature materials* **2015**, *14*, 473−477.

(14) Kou, X.; Guo, S.-T.; Fan, Y.; Pan, L.; Lang, M.; Jiang, Y.; Shao, Q.; Nie, T.; Murata, K.; Tang, J.; et al. Scale-Invariant Quantum Anomalous Hall Effect in Magnetic Topological Insulators Beyond the Two-Dimensional Limit. *Physical review letters* **2014**, *113*, 137201.

(15) Varykhalov, A.; Sánchez-Barriga, J.; Marchenko, D.; Hlawenka, P.; Mandal, P.; Rader, O. Tunable Fermi Level and Hedgehog Spin Texture in Gapped Graphene. *Nat. Commun.* **2015**, *6*, 7610.

(16) Wang, E.; Ding, H.; Fedorov, A. V.; Yao, W.; Li, Z.; Lv, Y.-F.; Zhao, K.; Zhang, L.-G.; Xu, Z.; Schneeloch, J.; et al. Fully Gapped Topological Surface States in Bi_2Se_3 Films Induced by a D-Wave High-Temperature Superconductor. *Nat. Phys.* **2013**, *9*, 621−625.

(17) Barfuss, A.; Dudy, L.; Scholz, M. R.; Roth, H.; Höpfner, P.; Blumenstein, C.; Landolt, G.; Dil, J.; Plumb, N.; Radovic, M.; et al. Elemental Topological Insulator With Tunable Fermi Level: Strained α-Sn on *InSb*(001). *Physical review letters* **2013**, *111*, 157205.

(18) Kellner, J.; Eschbach, M.; Kampmeier, J.; Lanius, M.; Młyńczak, E.; Mussler, G.; Holländer, B.; Plucinski, L.; Liebmann, M.; Grützmacher, D.; et al. Tuning the Dirac Point to The Fermi Level in The Ternary Topological Insulator. *Appl. Phys. Lett.* **2015**, *107*, 251603.

(19) Neupane, M.; Xu, S.-Y.; Wray, L. A.; Petersen, A.; Shankar, R.; Alidoust, N.; Liu, C.; Fedorov, A.; Ji, H.; Allred, J. M.; et al. Topological Surface States and Dirac Point Tuning in Ternary Topological Insulators. *Phys. Rev. B* **2012**, *85*, 235406.

(20) He, Q. L.; Pan, L.; Stern, A. L.; Burks, E. C.; Che, X.; Yin, G.; Wang, J.; Lian, B.; Zhou, Q.; Choi, E. S.; et al. Chiral Majorana Fermion Modes in a Quantum Anomalous Hall Insulator−Superconductor Structure. *Science* **2017**, *357*, 294−299.

(21) Klimovskikh, I. I.; Estyunin, D. A.; Makarova, T. P.; Tereshchenko, O. E.; Kokh, K. A.; Shikin, A. M. Electronic Structure of Pb Adsorbed Surfaces of Intrinsic Magnetic Topological Insulators. *journal of physical chemistry letters* **2022**, *13*, 6628−6634.

(22) Chen, Y.; Chu, J.-H.; Analytis, J.; Liu, Z.; Igarashi, K.; Kuo, H.-H.; Qi, X.; Mo, S.-K.; Moore, R.; Lu, D.; et al. Massive Dirac Fermion on the Surface of a Magnetically Doped Topological Insulator. *Science* **2010**, *329*, 659−662.

(23) Bobkova, I.; Bobkov, A. Electrically Controllable Spin Filtering Based on Superconducting Helical States. *Phys. Rev. B* **2017**, *96*, 224505.

(24) Xue, H.; Lv, W.; Wu, D.; Cai, J.; Ji, Z.; Zhang, Y.; Zeng, Z.; Jin, Q.; Zhang, Z. Temperature Dependence of Spin−Orbit Torques in Nearly Compensated $Tb_{21}Co_{79}$ Films by a Topological Insulator Sb_2Te_3. *J. Phys. Chem. Lett.* **2021**, *12*, 2394−2399.

(25) Cho, S.; Dellabetta, B.; Yang, A.; Schneeloch, J.; Xu, Z.; Valla, T.; Gu, G.; Gilbert, M. J.; Mason, N. Symmetry Protected Josephson Supercurrents in Three-Dimensional Topological Insulators. *Nat. Commun.* **2013**, *4*, 1689.

(26) Ghatak, S.; Breunig, O.; Yang, F.; Wang, Z.; Taskin, A. A.; Ando, Y. Anomalous Fraunhofer Patterns in Gated Josephson Junctions Based on the Bulk-Insulating Topological Insulator $BiSbTeSe_2$. *Nano Lett.* **2018**, *18*, 5124−5131.

(27) Yano, R.; Kudriashov, A.; Hirose, H. T.; Tsuda, T.; Kashiwaya, H.; Sasagawa, T.; Golubov, A. A.; Stolyarov, V. S.; Kashiwaya, S. Magnetic Gap of Fe-Doped $BiSbTe_2Se$ Bulk Single Crystals Detected by Tunneling Spectroscopy and Gate-Controlled Transports. *J. Phys. Chem. Lett.* **2021**, *12*, 4180−4186.

(28) Stolyarov, V. S.; Roditchev, D.; Gurtovoi, V. L.; Kozlov, S. N.; Yakovlev, D. S.; Skryabina, O. V.; Vinokur, V. M.; Golubov, A. A. Resonant Oscillations of Josephson Current in Nb-$Bi_2Te_{2.3}Se_{0.7}$-Nb Junctions. *Advanced Quantum Technologies* **2022**, *5*, 2100124.

(29) Stehno, M. P.; Ngabonziza, P.; Myoren, H.; Brinkman, A. Josephson Effect and Charge Distribution in Thin Bi_2Te_3 Topological Insulators. *Adv. Mater.* **2020**, *32*, 1908351.
(30) De Ronde, B.; Li, C.; Huang, Y.; Brinkman, A. Induced Topological Superconductivity in a $BiSbTeSe_2$-Based Josephson Junction. *Nanomaterials* **2020**, *10*, 794.
(31) Chen, Y.; Analytis, J. G.; Chu, J.-H.; Liu, Z.; Mo, S.-K.; Qi, X.-L.; Zhang, H.; Lu, D.; Dai, X.; Fang, Z.; et al. Experimental Realization of a Three-Dimensional Topological Insulator, Bi_2Te_3. *science* **2009**, *325*, 178−181.
(32) Stolyarov, V. S.; Pons, S.; Vlaic, S.; Remizov, S. V.; Shapiro, D. S.; Brun, C.; Bozhko, S. I.; Cren, T.; Menshchikova, T. V.; Chulkov, E. V.; et al. Superconducting Long-Range Proximity Effect through the Atomically Flat Interface of a Bi_2Te_3 Topological Insulator. *J. Phys. Chem. Lett.* **2021**, *12*, 9068−9075.
(33) Valdés Aguilar, R.; Wu, L.; Stier, A.; Bilbro, L.; Brahlek, M.; Bansal, N.; Oh, S.; Armitage, N. P. Aging and Reduced Bulk Conductance in Thin Films of the Topological Insulator Bi_2Se_3. *J. Appl. Phys.* **2013**, *113*, 153702.
(34) Goncalves, P. H.; Chagas, T.; Nascimento, V.; Dos Reis, D.; Parra, C.; Mazzoni, M.; Malachias, A.; Magalhães-Paniago, R. Formation of Bi_xSe_y Phases Upon Annealing of the Topological Insulator Bi_2Se_3: Stabilization of In-Depth Bismuth Bilayers. *J. Phys. Chem. Lett.* **2018**, *9*, 954−960.
(35) Scanlon, D.; King, P.; Singh, R. P.; De La Torre, A.; Walker, S. M.; Balakrishnan, G.; Baumberger, F.; Catlow, C. Controlling Bulk Conductivity in Topological Insulators: Key Role of Anti-Site Defects. *Adv. Mater.* **2012**, *24*, 2154−2158.
(36) Wang, L.-L.; Johnson, D. D. Ternary Tetradymite Compounds as Topological Insulators. *Phys. Rev. B* **2011**, *83*, 241309.
(37) Shekhar, C.; ViolBarbosa, C.; Yan, B.; Ouardi, S.; Schnelle, W.; Fecher, G. H.; Felser, C. Evidence of Surface Transport and Weak Antilocalization in a Single Crystal of the Bi_2Te_2Se Topological Insulator. *Phys. Rev. B* **2014**, *90*, 165140.
(38) Durand, C.; Zhang, X.-G.; Hus, S. M.; Ma, C.; McGuire, M. A.; Xu, Y.; Cao, H.; Miotkowski, I.; Chen, Y. P.; Li, A.-P. Differentiation of Surface and Bulk Conductivities in Topological Insulators via Four-Probe Spectroscopy. *Nano Lett.* **2016**, *16*, 2213−2220.
(39) Miyamoto, K.; Kimura, A.; Okuda, T.; Miyahara, H.; Kuroda, K.; Namatame, H.; Taniguchi, M.; Eremeev, S.; Menshchikova, T. V.; Chulkov, E. V.; et al. Topological Surface States with Persistent High Spin Polarization across the Dirac Point in Bi_2Te_2Se and Bi_2Se_2Te. *Physical review letters* **2012**, *109*, 166802.
(40) Chen, Q.; Su, K.; Li, Z.; Zhao, Z.; Hao, Y. $Bi_{1.9}Me_{0.1}Te_3$ Nanocrystal Functionalized Diamagnetic Glasses: Optical, Luminescence, Magnetic and Faraday Rotation. *J. Non-Cryst. Solids* **2020**, *543*, 120092.
(41) Zhukova, E. S.; Zhang, H.; Martovitskiy, V. P.; Selivanov, Y. G.; Gorshunov, B. P.; Dressel, M. Infrared Optical Conductivity of Bulk Bi_2Te_2Se. *Crystals* **2020**, *10*, 553.
(42) Jia, S.; Beidenkopf, H.; Drozdov, I.; Fuccillo, M.; Seo, J.; Xiong, J.; Ong, N. P.; Yazdani, A.; Cava, R. J. Defects and High Bulk Resistivities in the *Bi*-rich Tetradymite Topological Insulator-$Bi_{(2+x)}Te_{(2-x)}Se$. *Phys. Rev. B* **2012**, *86*, 165119.
(43) Nurmamat, M.; Krasovskii, E.; Kuroda, K.; Ye, M.; Miyamoto, K.; Nakatake, M.; Okuda, T.; Namatame, H.; Taniguchi, M.; Chulkov, E. V.; et al. Unoccupied Topological Surface State in Bi_2Te_2Se. *Phys. Rev. B* **2013**, *88*, 081301.
(44) Stephen, G. M.; Vail, O. A.; Lu, J.; Beck, W. A.; Taylor, P. J.; Friedman, A. L. Weak Antilocalization and Anisotropic Magnetoresistance as a Probe of Surface States in Topological $Bi_2Te_xSe_{3-x}$ Thin Films. *Sci. Rep.* **2020**, *10*, 4845.
(45) Kong, D.; Chen, Y.; Cha, J. J.; Zhang, Q.; Analytis, J. G.; Lai, K.; Liu, Z.; Hong, S. S.; Koski, K. J.; Mo, S.-K.; et al. Ambipolar Field Effect in the Ternary Topological Insulator $Bi_xSb_{(1-x)})_2Te_3$ by Composition Tuning. *Nature Nanotechnol.* **2011**, *6*, 705−709.
(46) Zhang, J.; Chang, C.-Z.; Zhang, Z.; Wen, J.; Feng, X.; Li, K.; Liu, M.; He, K.; Wang, L.; Chen, X.; et al. Band Structure Engineering in $Bi_xSb_{(1-x)})_2Te_3$ Ternary Topological Insulators. *Nat. Commun.* **2011**, *2*, 574.
(47) Miyamoto, K.; Okuda, T.; Nurmamat, M.; Nakatake, M.; Namatame, H.; Taniguchi, M.; Chulkov, E. V.; Kokh, K.; Tereshchenko, O.; Kimura, A. The Gigantic Rashba Effect of Surface States Energetically Buried in the Topological Insulator Bi_2Te_2Se. *New J. Phys.* **2014**, *16*, 065016.
(48) Hong, S. S.; Kundhikanjana, W.; Cha, J. J.; Lai, K.; Kong, D.; Meister, S.; Kelly, M. A.; Shen, Z.-X.; Cui, Y. Ultrathin Topological Insulator Bi_2Se_3 Nanoribbons Exfoliated by Atomic Force Microscopy. *Nano Lett.* **2010**, *10*, 3118−3122.
(49) Goyal, V.; Teweldebrhan, D.; Balandin, A. A. Mechanically-Exfoliated Stacks of Thin Films of Bi_2Te_3 Topological Insulators With Enhanced Thermoelectric Performance. *Appl. Phys. Lett.* **2010**, *97*, 133117.
(50) Ambrosi, A.; Sofer, Z.; Luxa, J.; Pumera, M. Exfoliation of Layered Topological Insulators Bi_2Se_3 and Bi_2Te_3 Via Electrochemistry. *ACS Nano* **2016**, *10*, 11442−11448.
(51) Sun, Z.; James, D. K.; Tour, J. M. Graphene Chemistry: Synthesis and Manipulation. *J. Phys. Chem. Lett.* **2011**, *2*, 2425−2432.
(52) Zhao, S.; Beekman, C.; Sandilands, L.; Bashucky, J.; Kwok, D.; Lee, N.; LaForge, A.; Cheong, S.-W.; Burch, K. Fabrication and Characterization of Topological Insulator Bi_2Se_3 Nanocrystals. *Appl. Phys. Lett.* **2011**, *98*, 141911.
(53) Charpentier, S.; Galletti, L.; Kunakova, G.; Arpaia, R.; Song, Y.; Baghdadi, R.; Wang, S. M.; Kalaboukhov, A.; Olsson, E.; Tafuri, F.; et al. Induced Unconventional Superconductivity on The Surface States of Bi_2Te_3 Topological Insulator. *Nat. Commun.* **2017**, *8*, 2019.
(54) Xue, H.; Yang, H.; Wu, Y.; Yao, G.; Guan, D.; Wang, S.; Zheng, H.; Liu, C.; Li, Y.; Jia, J. Molecular Beam Epitaxy of Superconducting $PdTe_2$ Films on Topological Insulator Bi_2Te_3. *Sci. China Phys. Mech. Astron.* **2019**, *62*, 76801.
(55) Schüffelgen, P.; Rosenbach, D.; Li, C.; Schmitt, T. W.; Schleenvoigt, M.; Jalil, A. R.; Schmitt, S.; Kölzer, J.; Wang, M.; Bennemann, B.; et al. Selective Area Growth and Stencil Lithography for in Situ Fabricated Quantum Devices. *Nature Nanotechnol.* **2019**, *14*, 825−831.
(56) Peng, H.; Lai, K.; Kong, D.; Meister, S.; Chen, Y.; Qi, X.-L.; Zhang, S.-C.; Shen, Z.-X.; Cui, Y. Aharonov−Bohm Interference in Topological Insulator Nanoribbons. *Nature materials* **2010**, *9*, 225−229.
(57) Cha, J. J.; Williams, J. R.; Kong, D.; Meister, S.; Peng, H.; Bestwick, A. J.; Gallagher, P.; Goldhaber-Gordon, D.; Cui, Y. Magnetic Doping and Kondo Effect in Bi_2Se_3 Nanoribbons. *Nano Lett.* **2010**, *10*, 1076−1081.
(58) Kong, D.; Dang, W.; Cha, J. J.; Li, H.; Meister, S.; Peng, H.; Liu, Z.; Cui, Y. Few-layer Nanoplates of Bi_2Se_3 and Bi_2Te_3 with Highly Tunable Chemical Potential. *Nano Lett.* **2010**, *10*, 2245−2250.
(59) Schönherr, P.; Collins-McIntyre, L. J.; Zhang, S.; Kusch, P.; Reich, S.; Giles, T.; Daisenberger, D.; Prabhakaran, D.; Hesjedal, T. Vapour-Liquid-Solid Growth of Ternary Bi_2Se_2Te Nanowires. *Nanoscale Res. Lett.* **2014**, *9*, 127.
(60) Lee, H.-Y.; Chen, Y.-S.; Lin, Y.-C.; Wu, J.-K.; Lee, Y.-C.; Wu, B.-K.; Chern, M.-Y.; Liang, C.-T.; Chang, Y. H. Epitaxial Growth of Bi_2Te_3 Topological Insulator Thin Films by Temperature-Gradient Induced Physical Vapor Deposition (*PVD*). *J. Alloys Compd.* **2016**, *686*, 989−997.
(61) Stolyarov, V. S.; Yakovlev, D. S.; Kozlov, S. N.; Skryabina, O. V.; Lvov, D. S.; Gumarov, A. I.; Emelyanova, O. V.; Dzhumaev, P. S.; Shchetinin, I. V.; Hovhannisyan, R. A.; et al. Josephson Current Mediated by Ballistic Topological States in $Bi_2Te_{2.3}Se_{0.7}$ Single Nanocrystals. *Commun. Mater.* **2020**, *1*, 38.
(62) Sharma, A.; Senguttuvan, T. D.; Ojha, V. N.; Husale, S. Novel Synthesis of Topological Insulator Based Nanostructures (Bi_2Te_3) Demonstrating High Performance Photodetection. *Sci. Rep.* **2019**, *9*, 3804.
(63) Lin, C.-H. Oxidation of Silicon. In *Encyclopedia of Microfluidics and Nanofluidics*; Li, D., Ed.; Springer: New York, NY, 2008.

https://doi.org/10.1021/acs.jpclett.2c02664
J. Phys. Chem. Lett. 2022, 13, 9221−9231

(64) Kanagaraj, M.; Pawbake, A.; Sarma, S. C.; Rajaji, V.; Narayana, C.; Measson, M.-A.; Peter, S. C. Structural, Magnetotransport and Hall Coefficient Studies in Ternary Bi_2Te_2See, Sb_2Te_2Se and Bi_2Te_2S Tetradymite Topological Insulating Compounds. *J. Alloys Compd.* **2019**, *794*, 195−202.
(65) Wang, K.; Graf, D.; Petrovic, C.; et al. Large Magnetothermopower and Fermi Surface Reconstruction in Sb_2Te_2Se. *Phys. Rev. B* **2014**, *89*, 125202.
(66) Denton, A. R.; Ashcroft, N. W. Vegard's Law. *Phys. Rev. A* **1991**, *43*, 3161.
(67) Liu, M.; Zhang, J.; Chang, C.-Z.; Zhang, Z.; Feng, X.; Li, K.; He, K.; Wang, L.-l.; Chen, X.; Dai, X.; et al. Crossover Between Weak Antilocalization and Weak Localization in a Magnetically Doped Topological Insulator. *Physical review letters* **2012**, *108*, 036805.
(68) Kim, Y. S.; Brahlek, M.; Bansal, N.; Edrey, E.; Kapilevich, G. A.; Iida, K.; Tanimura, M.; Horibe, Y.; Cheong, S.-W.; Oh, S. Thickness-Dependent Bulk Properties and Weak Antilocalization Effect in Topological Insulator Bi_2Se_3. *Phys. Rev. B* **2011**, *84*, 073109.

https://doi.org/10.1021/acs.jpclett.2c02664
J. Phys. Chem. Lett. 2022, 13, 9221−9231